

Local Structure of Epitaxial Single Crystal UO_{2+x} Thin Films

Jarrod C. Lewis^{1,*}, Steven D. Conradson^{2,3}, Jacek Wasik¹, Lottie M. Harding¹, Rebecca Nicholls¹, Jude Laverock⁴, Chris Bell¹, and Ross Springell¹

¹School of Physics, University of Bristol, Bristol, BS8 1TL, UK.

²Department of Complex Matter, Josef Stefan Institute, 100 Ljubljana, Slovenia.

³School of Chemistry, University of Bristol, Bristol, BS8 1TS, UK.

⁴Department of Chemistry, Washington State University, Pullman, WA 99164, USA.

*Current address: Department of Materials, University of Oxford, Oxford, OX1 3PH, UK.

Abstract

The influence of oxygen stoichiometry on the uranium local environment is explored in epitaxial single crystal uranium oxide thin films grown by DC magnetron sputtering. Through post-growth annealing, the stoichiometry of as-grown UO_2 films are tuned over an approximate stoichiometry range of $0.07 \leq x \leq 0.20$, estimated with X-ray photoelectron spectroscopy measurements of the U-4f and O-1s peaks. The local structure of the thin films are then probed using extended X-ray absorption fine structure measurements at the U L_3 absorption edge. We observe both the evolution of the U local environment of as a function of oxidation in UO_{2+x} , and that the near stoichiometric UO_2 film replicates the local structure of bulk UO_2 material standards well. The series of stoichiometrically varied samples highlights the non-trivial transitional behaviour of the UO_{2+x} oxygen sublattice with increasing oxygen content in this stoichiometric regime, while also demonstrating the efficacy of this thin film synthesis route for actinide studies beyond their established use as idealised surfaces, which could be readily adapted for further stoichiometrically tailored material studies and UO_{2+x} device fabrication.

1 Introduction

The binary uranium oxide phase diagram is rich in both structural diversity and chemical complexity [1, 2], with continuing developments even after decades of study [3–6]. The evolution of material properties with the variation of oxide stoichiometry x for a parent compound of UO_{2+x} is a substantial body of work. Recently there are a number of reports noting the possible utility of these oxygen content-dependent behaviours for the design of functional materials and devices [7–13]. Of particular interest is the stoichiometric range of $0 < x < 0.67$, which is bound on either end by the single-valence U(IV) face-centred cubic UO_2 phase ($x = 0$, space group $Fm\bar{3}m$), and the mixed-valence U(V)/U(VI) orthorhombic U_3O_8 phase ($x = 0.67$, space group $C2mm$) [14–16]. The magnetic, optical and electronic structure properties of both UO_2 [17–25] and U_3O_8 [26–28] attract continued research interest from a fundamental material science perspective. For UO_{2+x} between these two stoichiometric compounds the picture is less clear. New insights are frequently reported,

related to both the crystal structures adopted by the material, and the properties associated with the variation the U local environment with changing oxygen content [29–33].

However, it can be challenging to relate observations made using different uranium oxide sample morphologies, such as sintered powders and bulk single crystals. While powder based synthesis routes with rich microstructural variation continue to attract attention due to their intrinsic alignment to studies of nuclear fuel materials, work with solid crystalline samples is much less prolific, in part motivated by how challenging both growing and handling bulk single crystals of actinide materials can be. As such, there is continued interest in exploring how the rich material physics reported in sintered material systems with varying oxygen content manifests within uranium oxide materials with extended crystalline ordering, particularly in the UO_{2+x} stoichiometry regime.

To study solid UO_{2+x} , we synthesise epitaxial thin film single crystals, providing highly ordered systems in which to study small structural variations without the requirement of uniform bulk crystals. Following initial characterisation of the as-grown crystal structure with X-ray diffraction (XRD), and valence state characterisation using X-ray photoelectron spectroscopy (XPS), we studied the volume average local structure of a series of UO_{2+x} thin films. This made use of X-ray absorption fine structure (XAFS) measurements at the U L_3 absorption edge ($E = 17.166$ keV), and analysis of the extended X-ray absorption fine structure (EXAFS) oscillations within the X-ray fluorescence signal. The inter-atomic distances within the sample are characterised both as a function of the annealing treatment and sample temperature during the measurements. These are then fitted with a stoichiometric UO_2 single-scattering model to probe the variation in the local structure of the thin film from that of stoichiometric UO_2 .

We have also made similar measurements for bulk powder UO_2 to explore the ability of these thin films to replicate the bulk local structure. Through this combination of characterisation techniques, it is demonstrated that this epitaxial thin film synthesis route enables the replication of the complex anionic behaviour observed in the bulk material, and that this is further tuneable by post growth annealing.

2 Experimental Details

The samples were grown by reactive DC magnetron sputtering from a depleted uranium target in an ultra-high vacuum deposition chamber with a base pressure of the order 10^{-8} Pa. This dedicated actinide deposition system is part of the FaRMS facility at the University of Bristol [34, 35]. All samples used calcium fluoride (CaF_2) single crystals as substrates, sourced from MTI Corp®, with dimensions of $10\text{ mm} \times 10\text{ mm} \times 0.5\text{ mm}$, and polished to optical grade with a root-mean-square surface roughness of $\leq 5\text{ \AA}$. The high degree of epitaxial matching between CaF_2 and stoichiometric UO_2 facilitates epitaxial growth with minimal strain or crystallographic dislocations [36]. UO_2 layers were deposited on [111] or [100] oriented CaF_2 substrates, producing single crystal UO_2 thin films with corresponding orientations.

During UO_2 growth at a sputtering target power of 50 W, partial pressures of Ar and O_2 were maintained at 7.7×10^{-1} and 4×10^{-3} Pa respectively, and the substrate temperature was fixed at 500°C. The substrate was annealed at this temperature for 1 hour prior to deposition to desorb any surface contaminants and to thermalise the substrate. To provide a sufficient signal amplitude for fluorescence XAFS measurements, layers were grown to a nominal thickness of 500 nm, as calibrated using X-ray reflectivity to a rate of $\approx 3.8\text{ nm s}^{-1}$. Samples of nominal initial UO_2 ($x = 0$) stoichiometry were annealed to alter the oxygen content of the thin film using one of two

set ups. For characterisation in XRD and XAFS experiments, samples were annealed under various conditions detailed in Table 1 on a heated sample stage inside of an Anton Paar HTK-1200N high temperature oven.

Treatment	Anneal [mins]	Vacuum [Pa]	O_2 [Pa]	Temperature [°C]	[hkl]
SN1	720	1×10^{-2}	—	350	[111]
SN2	10	—	2×10^4	150	[111]
SN3	30	—	2×10^4	150	[111]
SN4	30	—	2×10^4	150	[100]

Table 1: UO_{2+x} post growth thin film annealing conditions.

For the XPS, the same heat treatments were replicated by placing the samples in the hot zone of a tube furnace under flowing O_2 for treatments SN2–4, and by annealing under the base vacuum of the XPS characterisation chamber ($< 1 \times 10^{-9}$ Pa) to replicate the SN1 treatment. While care was taken to ensure consistent parameters were used in these two annealing approaches, some variation is unavoidable and this informs the subsequent analysis.

To establish the phase and crystal structure of the as-grown thin films, ex-situ XRD characterisation was carried out using a PANalytical X’Pert Pro MPD diffractometer with a Cu K_α tube source ($E = 8.04$ keV) with the samples mounted on a standard Eulerian cradle. For XRD characterisation in-situ to the annealing processes, an Anton Paar HTK-1200N high temperature oven was used where diffraction measurements were collected through a Kapton window.

Measurements of the U and O valence species were collected using XPS at the NanoESCA Facility (University of Bristol, UK). The U-4f and O-1s peaks were characterised using a monochromatic Al K_α X-ray source ($E = 1.4867$ keV), with data collected using a Scienta-Omicron Argus analyser with a pass energy of 20 eV. To avoid sampling the hyperstoichiometric surface layer known to form in UO_{2+x} systems [37, 38] the spectra of samples annealed in O_2 were collected before and after sputtering the surface for 2 minutes with Ar ions at 500 V (approximately 7 μ A total sputter flux) to probe below this ≈ 20 Å hyperstoichiometric surface “capping” layer. This sputtering time and acceleration voltage combination was chosen to minimise disruption to the underlying U:O stoichiometry that may arise due to preferential sputtering of O. Subsequent analysis relies on the approximation that this region is representative of the remaining bulk of the thin film, and so the calculated stoichiometry values are quoted as approximates. These stoichiometry estimates are calculated as the atomic ratio of the O-1s and U-4f peaks. All XPS data processing and fitting was completed using CasaXPS [39] using standard methods from contemporary studies [40–44]. Prior to extracting atomic ratios, data were corrected for the transmission function of the instrument, and theoretical atomic cross-sections [45] were used for relative sensitivity factors.

XAFS measurements were collected around the U L_3 absorption edge ($E = 17.166$ keV) at beam line 2-2 at the Stanford Synchrotron Radiation Lightsource, California USA, with the incident beam monochromated and calibrated using the K absorption edge of an yttrium foil standard ($E = 17.0384$ keV). Samples were mounted in a vacuum sealed cylinder inside of a liquid He cryostat for temperature dependent measurements between 5 – 300 K, with fluorescence spectra collected using a Si drift detector positioned at 45° relative to the sample normal. This detection mode is necessitated by the thin film morphology of the sample, as the millimetre thick substrate would attenuate any signal if detected in transmission mode. No beam damage to the samples was observed, and the spectra showed the expected shift in the absorption edge energy (≈ 1 eV) after

warming the sample from 5 – 300 K. Spectra were averaged over 20 repetitions to improve the signal-to-noise ratio of the observed EXAFS oscillations within the absorption data.

Diffraction peaks from the single crystal CaF_2 substrates were observed decorating the XAFS spectra, which if included in the energy range of the EXAFS signal processing would introduce erroneous components to the Fourier analysis. An illustrative example of such a feature is plotted in the Supplementary Information as Figure S1. To minimise the impact of these features on the results of this study, a conservative window in wavenumber k was chosen of $\Delta k = 3 – 8.8 \text{ \AA}^{-1}$. As such, the raw fluorescence spectra $\mu(E)$ measured in these experiments were normalised relative to pre-edge and post-edge intensity to provide the normalised absorption $\chi(E)$. The first derivative of the absorption edge intensity was used to define E_0 , from which the wavenumber k was calculated. $\chi(E)$ was then converted to $\chi(k)$, with the data within the previously detailed Δk range Fourier transformed to provide the absorption as a function of inter-atomic distance R from the absorbing U sites, $\chi(R)$. This normalisation and spectra processing methodology used standard procedures in the DEMETER software suite [46]. Multiple scattering path fits were then performed on the $\chi(R)$ within a range $\Delta R = 1 – 5 \text{ \AA}$ using FEF6 [47] to quantify inter-atomic distances, using a bulk stoichiometric UO_2 room temperature reference structure [48].

3 Results & Discussion

The results of this thin film synthesis, processing and characterisation experiment will be presented in two parts; first focussed on the as-grown and vacuum annealed thin films relative to bulk UO_2 , and then on the annealed samples series. Both will feature XRD and XAFS measurements, while the XPS measurements are presented as part of the UO_{2+x} study.

3.1 As-grown and vacuum annealed UO_2 thin films

The synthesis of epitaxial UO_2 single crystals using the employed method is well established [35, 49, 50], with the growth conditions employed reliably producing single crystal films with the desired crystallographic orientation. XRD data collected for one such film are shown in Figure 1, with Figure 1a plotting the $\theta – 2\theta$ scan utilised for phase identification of a [100] oriented UO_2 thin film with a calculated lattice parameter of $a_0 = 5.47 \pm 0.01 \text{ \AA}$. Figure 1b is an azimuthal ϕ scan over two off-specular reflections within the UO_2 thin film and CaF_2 substrate, highlighting the highly crystalline character and the epitaxial matching of the two layers.

EXAFS measurements of a nominally stoichiometric UO_2 thin film after vacuum annealing (blue data) relative to a bulk UO_2 reference sample (orange data) are plotted as Figure 2. The unfitted modulus of $\chi(R)$ for both samples is plotted along with the respective real components of $\chi(R)$ in Figure 2a. Despite the 20 K temperature offset between these two data sets, both sample morphologies reproduce the main spectral features well.

The plotted modulus of $\chi(R)$, which appears as an envelope to the real component of $\chi(R)$, is analogous to a partial pair-distribution function, with each peak in inter-atomic distance R corresponding to scattering off of a nearest neighbour atom to the absorbing U atoms. The agreement between the two sets of data of Figure 2a indicates that the local structure of the thin film and bulk powder samples are similar. The real component plot of Figure 2a highlights that the signals contributing to the similar moduli of $\chi(R)$ are subtly different, particularly in the $2 – 3.5 \text{ \AA}$ range, suggesting that different multiple scattering processes contribute towards the observed EXAFS in

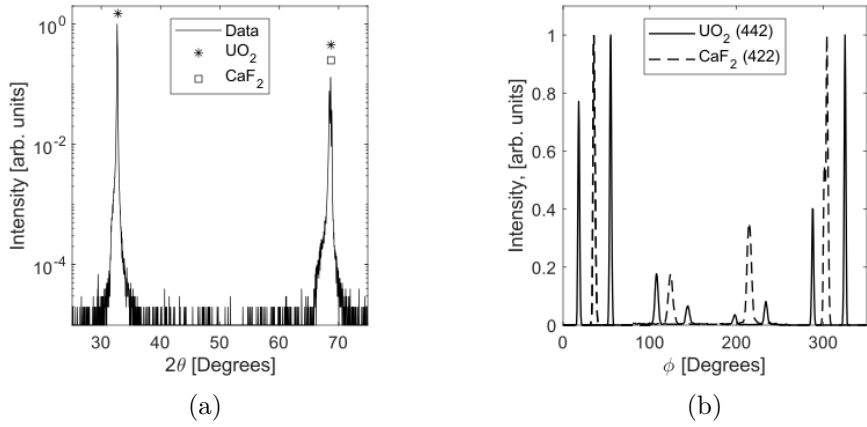


Figure 1: XRD of an epitaxial UO_2 thin film deposited onto a CaF_2 substrate. (a) A $\theta - 2\theta$ scan, with peak positions from both the thin film and substrate labelled with symbols. (b) An off-specular ϕ scan, showing reflections from the thin film (solid lines) and substrate (dashed lines).

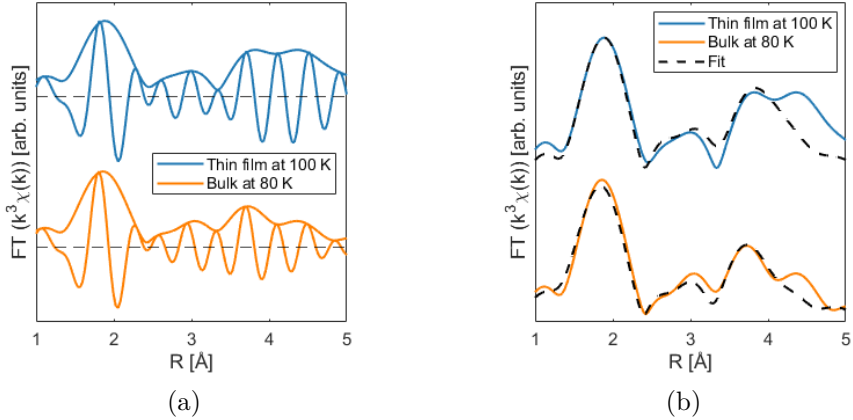


Figure 2: Fourier transformed U L_3 edge EXAFS $\chi(R)$ of a vacuum annealed epitaxial thin film UO_2 (blue) and bulk powder UO_2 (orange). (a) The modulus and real component of $\chi(R)$, with a dashed horizontal line representing the respective zero level. In the modulus the peaks correspond to scattering paths to nearest neighbours, while the real component of the Fourier transform highlights spectral components as a function of R . (b) The modulus of $\chi(R)$ shown relative to the multiple-scattering fit model (dashed lines).

the thin film relative to the bulk sample. In Figure 2b the modulus of $\chi(R)$ for the thin film and bulk UO_2 samples is fitted to the expected inter-atomic distances of UO_2 , showing that both data sets are well captured by the expected stoichiometric UO_2 local structure. The corresponding $\chi(k)$ representation of the data of Figure 2 is included in the Supplementary Information as Figure S2.

3.2 Annealed UO_{2+x} thin films

As-grown UO_2 thin films were processed as detailed in Table 1 to alter the oxygen content to see what affect this has on the crystal and local structure of the system. For the XRD and XAFS studies, the same sample batch was used with XRD characterisation carried out in-situ to the annealing process, with this plotted as Figure 3. Here it is evident that the as-grown material again has the expected face-centred cubic structure of UO_2 (black data, inset plot), but that on magnifying the scale over the (111) reflection, the impact of the annealing treatment is apparent.

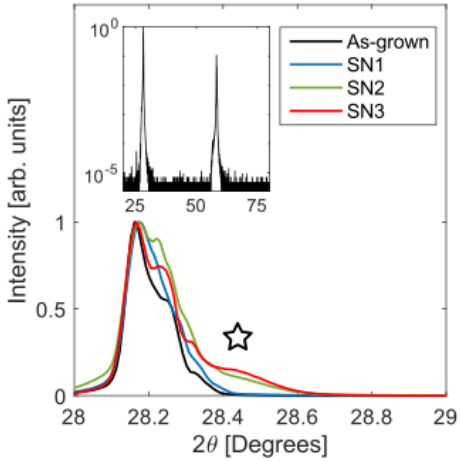


Figure 3: XRD of as-grown (black) UO_2 thin films with in-situ $\theta - 2\theta$ characterisation as a function of vacuum annealing (blue) and sequentially longer oxygen annealing treatments (green, red). A non-indexed peak (star) emerged with O_2 annealing.

Treatment	a_0 [\AA]
As-grown	5.47 ± 0.01
SN1	5.46 ± 0.03
SN2	5.47 ± 0.01
SN3	5.47 ± 0.06

Table 2: Lattice parameters calculated from XRD patterns for as-grown and annealed UO_2 thin films.

To reduce hyperstoichiometry in the as-grown thin film, the SN1 sample (blue data) was annealed under vacuum, resulting in the (111) reflection shifting to higher 2θ as the lattice contracts. Annealing in O_2 results in a minor broadening of the Bragg reflection, but no statistically significant shift in 2θ relative to the as-grown material is observed. The corresponding lattice parameters are calculated from pseudo-Voigt fits to the peak centres, and are tabulated as Table 2. Here it is evident that although the peaks in Figure 3 become marginally broader upon annealing in O_2 , there is not a shift in the cubic lattice parameter within the uncertainty of the measurement. It is notable that a secondary peak, marked by the star in Figure 3, grows with increasing O_2 annealing time, which is not commensurate with a distorted cubic UO_{2+x} structure.

The data of Figure 3 and the tabulated lattice parameters of Table 2 also indicate that the thin films have not undergone a phase transition, and that any difference to the crystal structure resulting of this treatment would be subtle. The lattice parameter of UO_2 is determined by the second nearest neighbour U-U inter-atomic distance, and thus it requires a considerable addition of interstitial O to influence the lattice parameter. From this XRD characterisation, we can surmise that any hyperstoichiometry in these epitaxial thin films for the SN2 – 3 sample treatments is low,

but this cannot be directly quantified by the information content of XRD.

To further explore the impact of these annealing treatments on the thin film oxygen content, the surface stoichiometry was investigated by characterising the U and O valence speciation with XPS for three UO_2 [111] oriented thin films processed in keeping with the samples characterised in Figure 3. The data for the O-1s characterisation of vacuum annealed (SN1) and annealed in oxygen and surface sputtered with Ar^+ ions (SN2 – 3) are plotted as Figure 4a-4c, with the corresponding U-4f data plotted as Figure 4d-4f. All fit parameters are tabulated as Table 3.

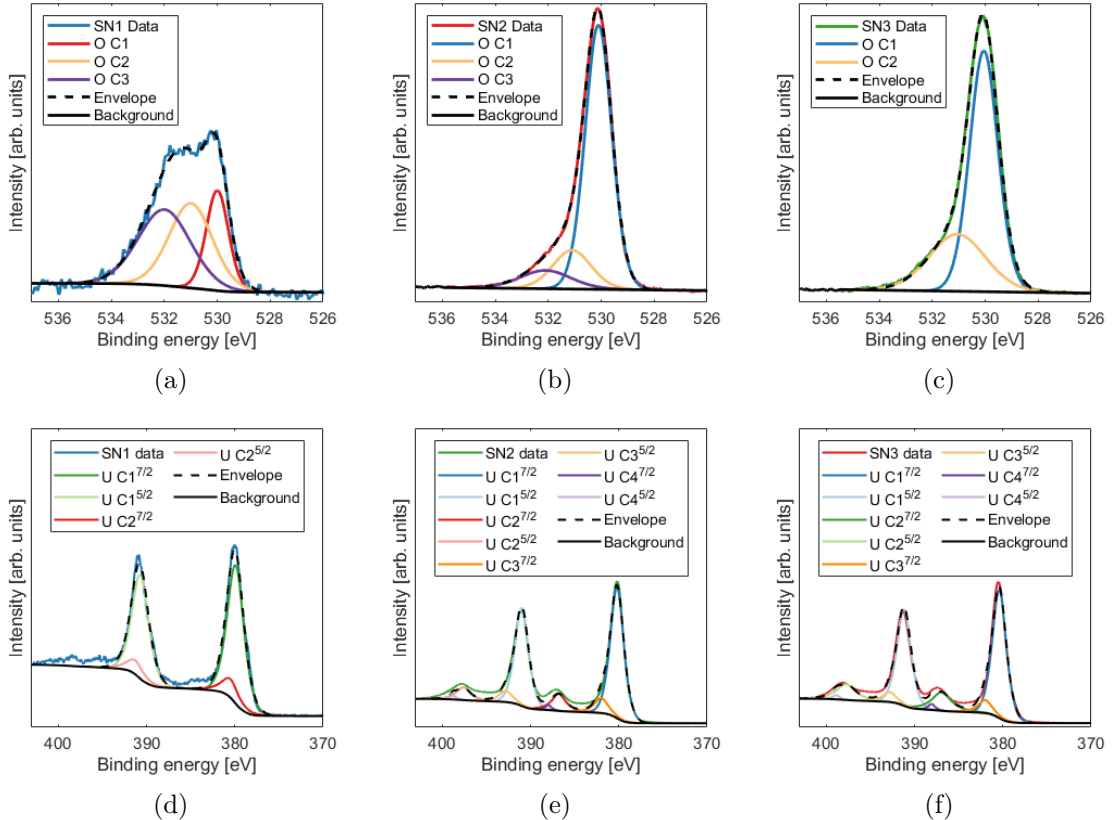


Figure 4: X-ray photoemission spectra characterisation of annealed UO_2 epitaxial thin films. (a-c) O-1s peak characterisation for SN1 – 3 respectively. (d-f) U-4f peak characterisation for SN1 – 3 respectively. Each fit makes use of a Shirley background profile. Component parameters are detailed in Table 3.

To aide comparison on spectral features, U-4f peaks, the O-1s peaks, and the estimated surface stoichiometry of the thin films are plotted as Figure 5. From inspection of Figure 5a, the SN1 data shows a significant attenuation of the U-4f signal relative to that of SN2 – 3, with no clear evidence of the satellite peaks. This corresponds well with the SN1 O-1s spectra in Figure 5b, which has a clear secondary peak component centred around $BE = 532$ eV in addition to a main component at $BE = 530$ eV attributed to the lattice O. This secondary component is attributed to physisorbed O species on the film surface, despite the vacuum conditions used for the annealing treatment. Upon annealing in O_2 and sputtering the surface, the U-4f peaks shift subtly but

Treatment	Component	Position [eV]	FWHM	% GL	O:U Ratio
SN1	U C1 $^{7/2}$	379.89	2.34	60	2.07 ± 0.04
	U C1 $^{5/2}$	390.69	2.34	60	
	U C2 $^{7/2}$	380.50	0.82	60	
	U C2 $^{5/2}$	391.30	0.82	60	
	O C1	529.99	0.96	30	
	O C2	530.98	2.16	30	
	O C3	532.00	2.47	30	
SN2	U C ₁ $^{7/2}$	380.21	1.83	60	2.17 ± 0.02
	U C ₁ $^{5/2}$	391.01	1.83	60	
	U C ₂ $^{7/2}$	382.58	1.83	60	
	U C ₂ $^{5/2}$	392.14	1.83	60	
	U C ₃ $^{7/2}$	380.21	1.87	60	
	U C ₃ $^{5/2}$	391.01	1.87	60	
	U C ₄ $^{7/2}$	382.58	0.71	60	
	U C ₄ $^{5/2}$	392.14	0.71	60	
	O C ₁	530.10	1.19	30	
	O C ₂	531.10	1.70	30	
SN3	O C ₃	532.10	2.27	30	2.20 ± 0.02
	U C ₁ $^{7/2}$	380.4	2.00	60	
	U C ₁ $^{5/2}$	391.2	2.00	60	
	U C ₂ $^{7/2}$	380.48	2.00	60	
	U C ₂ $^{5/2}$	391.68	2.00	60	
	U C ₃ $^{7/2}$	386.60	2.57	60	
	U C ₃ $^{5/2}$	397.4	2.57	60	
	U C ₄ $^{7/2}$	388.00	1.21	60	
	U C ₄ $^{5/2}$	398.40	1.21	60	
	O C ₁	530.05	1.26	30	
	O C ₂	531.05	2.45	30	

Table 3: Table of component parameters used in the fitting of the XPS data for the U-4f and O-1s peaks. Satellite peaks of the U-4f C1 and C2 components were modelled as C3 and C4 respectively, with $\Delta BE = 6 - 8$ eV. The O-1s components are interpreted as lattice (C1), chemisorbed (C2), and physisorbed (C3) O environments respectively.

adopt a more expected peak structure for a UO_{2+x} surface, while the O-1s spectral components becomes less clearly binary with the physisorbed component decreasing drastically, leaving a minor chemisorbed O shoulder at $BE = 531$ eV. next to the lattice O component by the SN3 treatment. Figures 5a-5b demonstrate the responsiveness of the thin films to the oxidation treatment, while also highlighting the limitations of this surface sensitive analysis technique for such reactive oxide species.

The surface stoichiometry of the epitaxial thin films are estimated as the ratio of the lattice O to U peak intensity, with the results of this analysis plotted as Figure 5c. Here it is evident that whilst SN1 has a lower estimated surface stoichiometry than the O_2 annealed samples, the reduced thin film retains a level of hyperstoichiometry of $x \approx 0.07$. This could be the result of the previously noted surface contamination of the O-1s peak influencing the detected intensity of the component assigned to the lattice oxygen, but it is difficult to be definitive for such surface sensitive measurements. The SN2 and SN3 samples show an increase in their respective surface stoichiometry estimates with annealing time, but neither is found to pass beyond $x \approx 0.20$, which is below the stoichiometry commonly associated with the onset to the U_4O_9 phase of $x \geq 0.25$. It is

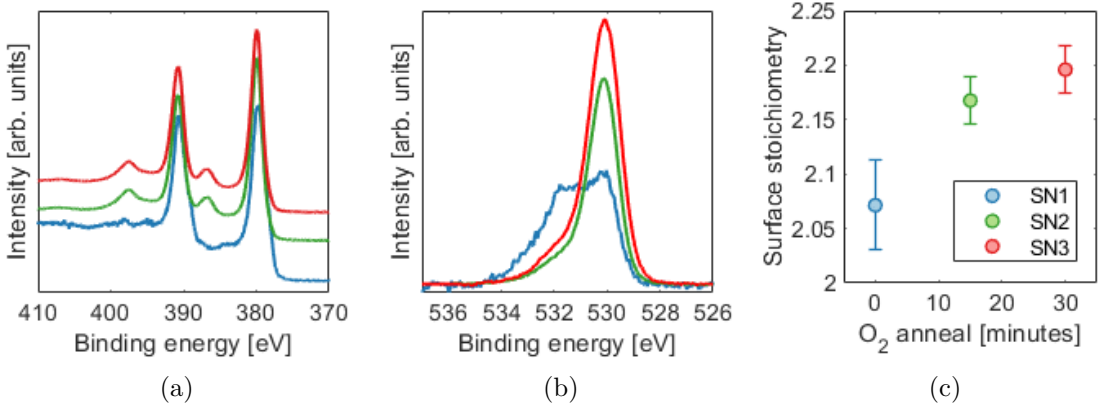


Figure 5: X-ray photoemission spectra characterisation of annealed UO_2 epitaxial thin films. Note the SN1 data (blue) in (a-b) have been scaled by a factor of $50\times$ to aide comparison. (a) U-4f peak characterisation. (b) O-1s peak characterisation. (c) Estimated surface stoichiometry from the fitted U-4f and O-1s peak areas.

noted that this analysis relies on accurate photoelectron cross-sections, and although uncertainties in this quantity may contribute a systematic error of $\approx 5\%$, the reported trend in the O:U ratio is robust.

The XAFS measurements of the U L_3 absorption edge are volume averaged, and thus analysis of the EXAFS within the XAFS signal provides a probe of the local structure that is not surface limited, with an inter-atomic distance sensitivity range of $R \leq 5.5 \text{ \AA}$. The magnitude of $\chi(R)$ for the three previously discussed sample treatments (SN1 – 3) are plotted as Figure 6, with each plot representing spectra collected at different sample temperatures. The fits to the data (dashed black lines) are limited to the U-O₁, U-U₁ and U-O₂ nearest neighbour scattering paths for pristine bulk UO_2 , and thus spectral weight unaccounted for by these fits is suggestive of scattering from non-stoichiometric atomic sites. The corresponding $\chi(k)$ representation of each of these data are included in the Supplementary Information as Figure S3.

The plots of Figure 6 highlight that at 5 K, the EXAFS shows a good agreement between the stoichiometric UO_2 scattering model for all samples between $1 - 5 \text{ \AA}$. As the sample temperature is increased, the agreement between the model and the data generally decreases, with the most disagreement seen in the SN2 data above 200 K. Notably, the SN3 data is particularly poorly fitted in the first peak, corresponding to scattering from the U-O₁ path, at 200 K (red data, Figure 6c).

The real component of $\chi(R)$, and the corresponding multiple scattering fits, are plotted for SN1 – 3 as Figure 7. In keeping with the trends observed in Figure 6, the agreement between the UO_2 multiple scattering model is higher at low temperature, with this generally decreasing as the temperature of the sample increases. Notably here the SN3 300 K data (red data, Figure 7d) shows a good agreement in the real component of $\chi(R)$, with SN2 showing a greater disagreement across the 200 – 300 K range. Importantly, the plots of Figure 7 highlight that each EXAFS measurement has distinct features that are not common to every sample, and that these evolve with the measurement temperature. This indicates that there is some reordering of the scattering sites within the material as the sample temperature changes, with different configurations being more or less well captured by the stoichiometric UO_2 model.

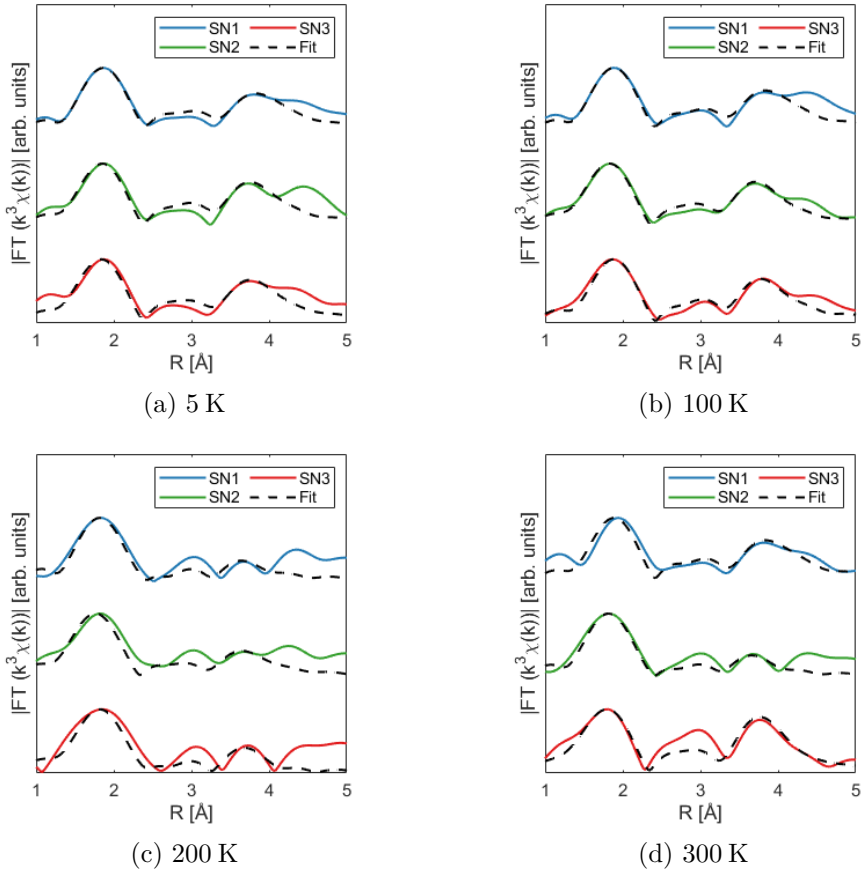


Figure 6: Magnitude of $\chi(R)$ for UO_{2+x} thin film samples SN1–3. Each plot shows spectra collected at different sample temperatures. Multiple-scattering fits are shown as dashed black lines, with the corresponding fit parameters tabulated in the Supplementary Information as Tables S1 – 3.

To further probe the temperature dependence of the EXAFS, a second sample was processed using the same treatment of SN3, grown on [100] oriented CaF_2 to see if the variation in substrate orientation influences the observed temperature dependence in the local structure. For clarity this sample is termed SN4, but experienced the same sample treatment as SN3 as previously detailed. These measurements were collected at finer temperature increments to better probe temperature dependent spectral evolution, but were otherwise measured using the same method as the spectra plotted in Figure 7 and Figure 8. The SN4 spectra are fitted with the same stoichiometric UO_2 model used for the SN1 – 3 analysis, to determine the deviation from the ideal UO_2 structure without allowing for additional scattering paths within the unit cell. The corresponding $\chi(R)$ measurements are plotted as Figure 8, with $\chi(k)$ plotted in the Supplementary Information as Figure S4.

Both the magnitude and real component of $\chi(R)$ plotted as Figures 8a and 8b respectively show a similar evolution with sample temperature as observed in the four sets of data plotted

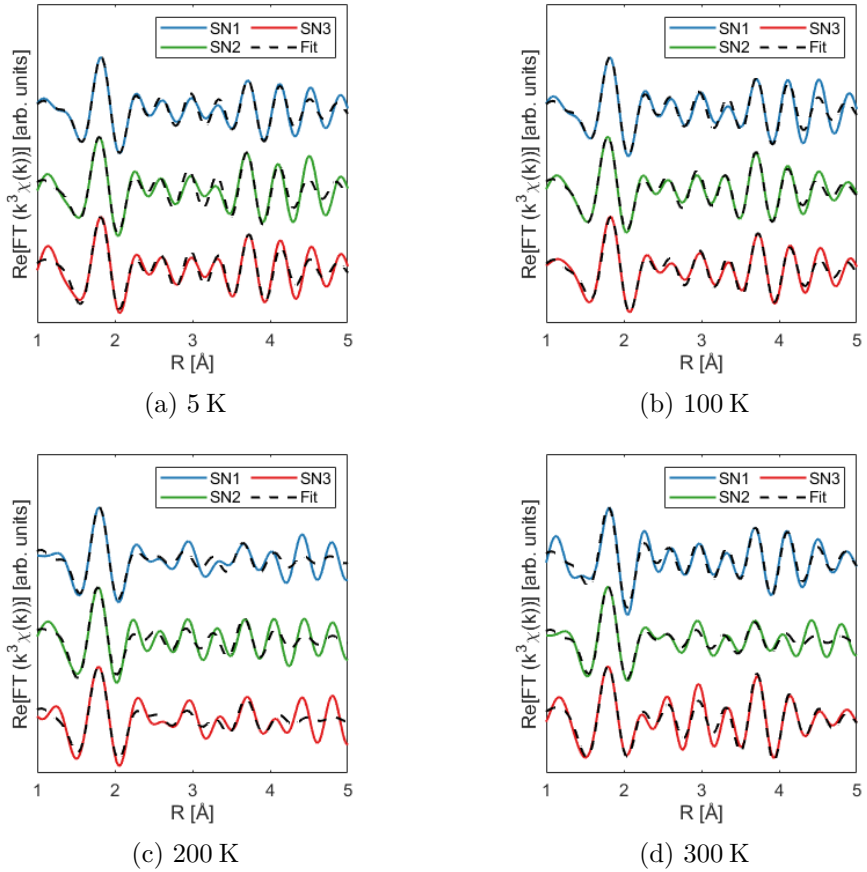


Figure 7: Real component of $\chi(R)$ for UO_{2+x} thin film samples SN1 – 3. Each plot shows spectra collected at different sample temperatures. Multiple-scattering fits to each of the spectra are included as dashed black lines.

for SN3 in Figures 6–7. In both of the representations of the data in Figure 8 there is a closer agreement between the UO_2 model and the data at low temperature and near room temperature, with the disagreement more pronounced in the 80–200 K range. While this appears more dramatic in the magnitude plot of Figure 8a, the real component representation of Figure 8b demonstrates that this arises due to new components in the Fourier transform emerging in this range of sample temperatures, which cannot be accounted for in this three scattering path UO_2 basis.

The quantitative output of the multiple scattering fits are tabulated in full in the Supplementary Information as Tables S1 – 4, but the fitted inter-atomic distances of the fits to samples SN1 – 4 for the three modelled scattering paths are plotted separately as Figure 9. Here the uncertainty on each data point is propagated from the FEFF6 fitting model, and the dashed horizontal lines correspond to the expected inter-atomic distance for that scattering path in bulk UO_2 at 300 K. Overall, the two O scattering paths are the most variable of the three included in these fits, with the U–O₂ path being notably more sensitive to both the O₂ annealing and the variation in the sample temperature during the measurement. This is markedly different from the nearest neighbour U–U₁

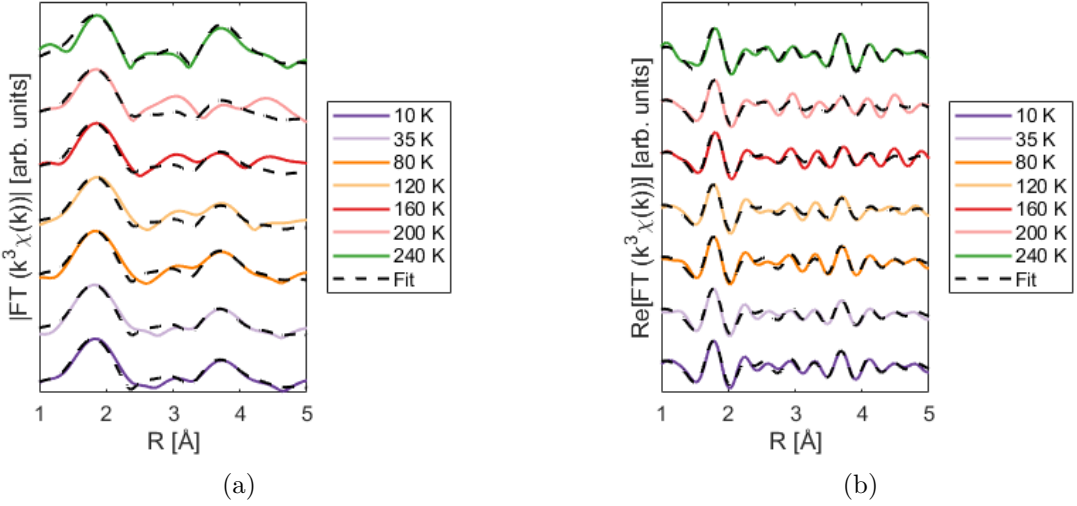


Figure 8: Absorption spectra for the UO_{2+x} thin film samples SN4, plotted as a function of sample temperature. The multiple-scattering fits to each of the spectra is included as dashed black lines. (a) Magnitude and (b) Real component, of the Fourier transformed absorption spectra, respectively.

scattering path, which is largely invariant from the expected stoichiometric inter-atomic distance for each of the fits, in keeping with the findings of the XRD analysis of these samples.

The inter-atomic distances fitted for SN1 agree with the bulk reference structure well, with the U-O₂ distance at 200 K being a notable variation from this relative invariance with sample temperature during the measurement. The inter-atomic distances for SN2 – 4 vary more notably from the bulk room temperature structure, with this most clearly manifesting in the U-O₂ distances, but also in the U-U and U-O₁ of SN2 and SN4. It is notable that the SN2 U-O₁ distance varies more from the stoichiometric value than the SN4 values do, indicating that the degree of distortion from the stoichiometric structure does not increase monotonically with increased oxidation.

Together, Figures 6-9 show the complexity of these mildly oxidised epitaxial thin film systems as viewed from the bulk averaged probe of XAFS, with the EXAFS analysis indicating that while the low temperature local structure appears closely aligned to that of stoichiometric UO_2 , the prominence of interstitial O sites becomes more apparent with elevated temperature. Furthermore, the U-U₁ behaviour corroborates the XRD analysis well, indicating the U sublattice behaves in a similar way in these epitaxial systems as is observed in the bulk material. Finally, the sensitivity of the local structure to sample temperature is notable, and hints at a dynamic quality to the O sublattice which is most readily observed after oxidative annealing.

4 Conclusions

This synthesis route for epitaxial uranium oxide systems has successfully produced phase pure UO_2 , which were then tailored to differing O content through annealing treatments. While the absolute degree of stoichiometry is non-trivial to determine using non-destructive methods, this

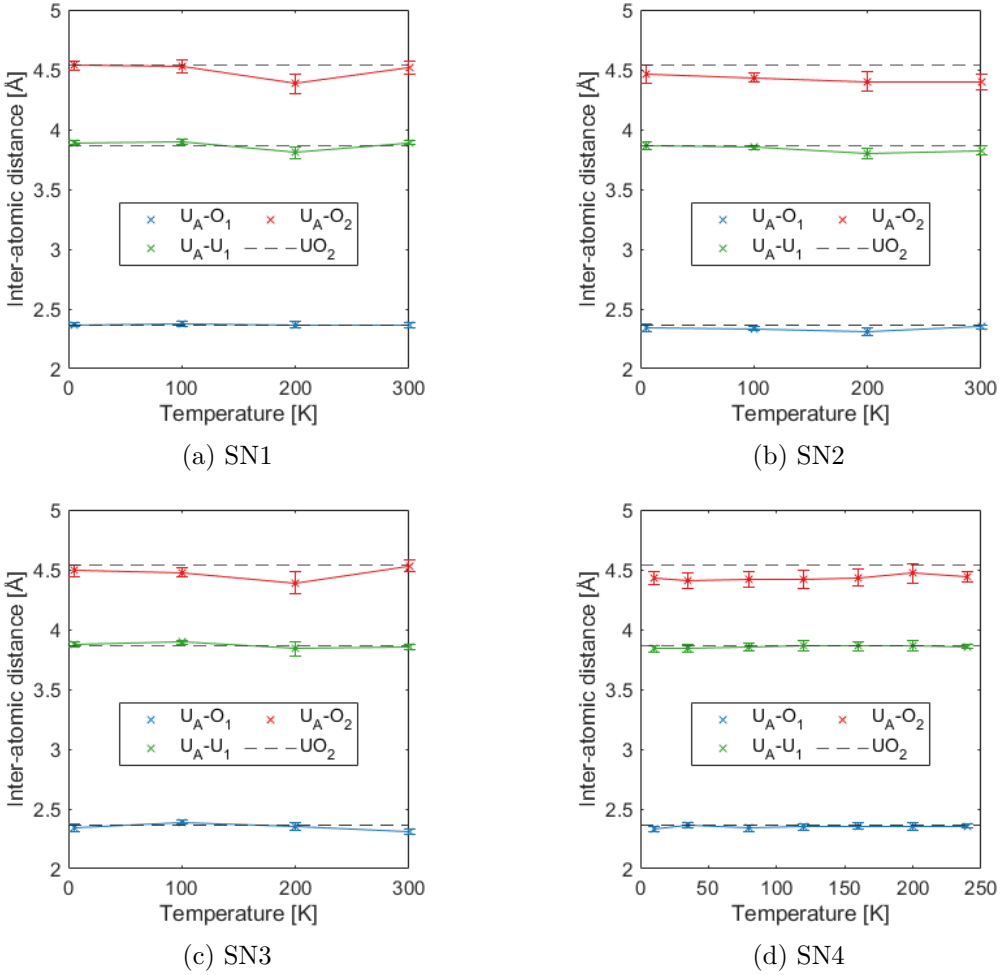


Figure 9: Fitted inter-atomic distances for the UO_{2+x} EXAFS. Here each modelled scattering path is shown relative to the room temperature value for bulk UO_2 , with the nearest neighbour U-O (blue) and U-U (green) paths and the second nearest neighbour U-O (red) path shown for various sample temperatures.

range of annealing treatments is estimated through XPS analysis to result in a stoichiometric range of $0.07 \leq x \leq 0.20$, and thus are not expected to show the U_4O_9 phase where $x \geq 0.25$. These samples instead occupy a transitional region of the UO_{2+x} phase diagram, where O clustering and interstitial O site occupancy are thought to drive the observed alterations to the material properties in the bulk. The variation in the local structure with both oxidation treatment and sample temperature during measurement as probed through the EXAFS analysis highlights the efficacy of this epitaxial thin film synthesis route in replicating the complex material character of the bulk material, and suggests that such epitaxial systems could be employed as proxies to the bulk in more convoluted material studies in which the use of bulk or powdered uranium oxide materials are prohibitive. Furthermore, the observed variation in the local structure with sample temperature is suggestive of a pronounced dynamic character to the interstitial sites within the

UO_{2+x} O sublattice, which has been suggested in other contemporary studies of the bulk material and powdered systems.

Acknowledgements

JCL was funded by the UKRI Engineering and Physical Sciences Research Council (EPSRC), through the Centre for Doctoral Training in Condensed Matter Physics (CDT-CMP) grant no. EP/L015544/1, with additional funding for this work from the Transformative Science and Engineering for Nuclear Decommissioning (TRANSCEND) consortium, grant no. EP/L014041/1. This work was further funded by the EPSRC NNUF FaRMS Facility, grant no. EP/V035495/1. Use of the Stanford Synchrotron Radiation Lightsource, SLAC National Accelerator Laboratory, is supported by the U.S. Department of Energy, Office of Science, Office of Basic Energy Sciences under contract no. DE-AC02-76SF00515. The authors also acknowledge use of the University of Bristol NanoESCA Laboratory.

Contributions

JCL (Conceptualization, Formal analysis, Investigation, Methodology, Writing – original draft, Writing - review & editing), SDC (Formal analysis, Investigation, Writing - review & editing), JW (Investigation, Writing - review & editing), LMH (Investigation, Writing - review & editing), RN (Investigation, Writing - review & editing), JL (Investigation, Writing - review & editing), CB (Conceptualization, Funding acquisition, Supervision, Writing – original draft, Writing – review & editing), RSS (Conceptualization, Funding acquisition, Supervision, Writing – review & editing).

References

- [1] R. McEachern and P. Taylor, “A review of the oxidation of uranium dioxide at temperatures below 400°C,” *Journal of Nuclear Materials*, vol. 254, no. 2-3, pp. 87–121, 1998.
- [2] H. Idriss, “Surface reactions of uranium oxide powder, thin films and single crystals,” *Surface Science Reports*, vol. 65, no. 3, pp. 67–109, 2010.
- [3] M. Baichi, C. Chatillon, K. Froment, M. Baichi, C. Chatillon, G. Ducros, and K. Froment, “Thermodynamics of the O–U system: III – Critical assessment of phase diagram data in the U– UO_{2+x} composition range,” *Journal of Nuclear Materials*, vol. 349, no. 1-2, pp. 57–82, 2006.
- [4] D. Prieur, M.-M. Desagulier, D. R. Neuville, C. Guéneau, E. Epifano, K. Dardenne, J. Rothe, and P. Martin, “A spectroscopic hike in the U-O phase diagram,” *Journal of Synchrotron Radiation*, vol. 28, no. 6, pp. 1684–1691, 2021.
- [5] J. Wasik, J. Sutcliffe, R. Podor, J. Lewis, J. E. Darnbrough, S. Rennie, S. Akbar Hussain, C. Bell, D. A. Chaney, G. Griffiths, L. M. Harding, F. Legg, E. Lawrence Bright, R. Nicholls, Y. Sasikumar, A. Siberry, P. Smith, and R. Springell, “Polyepitaxial grain matching to study the oxidation of uranium dioxide,” *npj Materials Degradation*, vol. 8, no. 1, p. 68, 2024.

- [6] C. L. Silva, L. Amidani, M. Retegan, S. Weiss, E. F. Bazarkina, T. Graubner, F. Kraus, and K. O. Kvashnina, “On the origin of low-valent uranium oxidation state,” *Nature Communications*, vol. 15, no. 1, p. 6861, 2024.
- [7] T. T. Meek and B. von Roedern, “Semiconductor devices fabricated from actinide oxides,” *Vacuum*, vol. 83, no. 1, pp. 226–228, 2008.
- [8] C. A. Kruschwitz, S. Mukhopadhyay, D. Schwellenbach, T. Meek, B. Shaver, T. Cunningham, and J. P. Auxier, “Semiconductor neutron detectors using depleted uranium oxide,” in *Proceedings of SPIE*, vol. 9213 of *SPIE Optical Engineering + Applications*, 2014.
- [9] C. Young, J. Petrosky, J. M. Mann, E. M. Hunt, D. Turner, and T. Kelly, “The work function of hydrothermally synthesized UO_2 and the implications for semiconductor device fabrication,” *Physica Status Solidi. Rapid Research Letters*, vol. 10, no. 9, pp. 687–690, 2016.
- [10] W. Liu, E. Song, L. Cheng, L. Song, J. Xie, G. Li, Y. Zhang, Y. Wang, Y. Wang, Z. Xia, Z. Chai, and S. Wang, “Introducing uranium as the activator toward highly stable narrow-band green emitters with near-unity quantum efficiency,” *Chemistry of Materials*, vol. 31, no. 23, pp. 9684–9690, 2019.
- [11] K. Rickert, T. A. Prusnick, M. A. Streby, D. B. Turner, C. J. Reyner, and J. M. Mann, “Point light detection with UO_2 ,” *Journal of Applied Physics*, vol. 130, no. 7, 2021.
- [12] L. Cheng, C. Liang, B. Li, H. Qin, P. Mi, B. Chen, Y. Yan, X. Dai, C. Zhang, Y. Wang, Y. Wang, and S. Wang, “Millimeter-scale semiconductive metal-organic framework single crystal for X-ray imaging,” *Cell Reports Physical Science*, vol. 3, no. 8, 2022.
- [13] J. Xie, H. Hou, H. Lu, F. Lu, W. Liu, X. Wang, L. Cheng, Y. Zhang, Y. Wang, Y. Wang, J. Diwu, B. Hu, Z. Chai, and S. Wang, “Photochromic uranyl-based coordination polymer for quantitative and on-site detection of UV radiation dose,” *Inorganic Chemistry*, vol. 62, no. 39, pp. 15834–15841, 2023.
- [14] G. Leinders, R. Bes, J. Pakarinen, K. Kvashnina, and M. Verwerft, “Evolution of the uranium chemical state in mixed-valence oxides,” *Inorganic Chemistry*, vol. 56, no. 12, pp. 6784–6787, 2017.
- [15] H. Hoekstra and S. Siegel, “The uranium-oxygen system: U_3O_8 - UO_3 ,” *Journal of Inorganic and Nuclear Chemistry*, vol. 18, pp. 154–165, 1961.
- [16] B. O. Loopstra, “The structure of β - U_3O_8 ,” *Acta Crystallographica Section B*, vol. 26, pp. 656–657, May 1970.
- [17] R. Caciuffo, P. Santini, S. Carretta, G. Amoretti, A. Hiess, N. Magnani, L.-P. Regnault, and G. H. Lander, “Multipolar, magnetic, and vibrational lattice dynamics in the low-temperature phase of uranium dioxide,” *Physical Review B*, vol. 84, no. 104409, 2011.
- [18] Y. Q. An, A. J. Taylor, S. D. Conradson, S. A. Trugman, T. Durakiewicz, and G. Rodriguez, “Ultrafast hopping dynamics of 5f electrons in the Mott insulator UO_2 studied by femtosecond pump-probe spectroscopy,” *Physical Review Letters*, vol. 106, no. 20, 2011.

[19] S. D. Conradson, T. Durakiewicz, F. J. Espinosa-Faller, Y. Q. An, D. A. Andersson, A. R. Bishop, K. S. Boland, J. A. Bradley, D. D. Byler, D. L. Clark, D. R. Conradson, L. L. Conradson, A. L. Costello, N. J. Hess, G. H. Lander, A. Llobet, and M. B. Martucci, “Possible Bose-condensate behavior in a quantum phase originating in a collective excitation in the chemically and optically doped Mott-Hubbard system UO_{2+x} ,” *Physical Review B*, vol. 88, no. 11, 2013.

[20] Z. Bao, R. Springell, H. C. Walker, H. Leiste, K. Kuebel, R. Prang, G. Nisbet, S. Langridge, R. C. C. Ward, T. Gouder, R. Caciuffo, and G. H. Lander, “Antiferromagnetism in UO_2 thin epitaxial films,” *Physical Review B*, vol. 88, no. 13, 2013.

[21] S. M. Gilbertson, T. Durakiewicz, G. L. Dakovski, Y. Li, J.-X. Zhu, S. D. Conradson, S. A. Trugman, and G. Rodriguez, “Ultrafast photoemission spectroscopy of the uranium dioxide UO_2 mott insulator: Evidence for a robust energy gap structure,” *Physical Review Letters*, vol. 112, no. 8, 2014-2-28.

[22] E. Tereshina, S. Daniš, R. Springell, Z. Bao, L. Havela, and R. Caciuffo, “Crystal structure and magnetic properties of UO_2 /permalloy thin films,” *Thin Solid Films*, vol. 591, pp. 271–275, 2015.

[23] S. D. Conradson, D. A. Andersson, P. S. Bagus, K. S. Boland, J. A. Bradley, D. D. Byler, D. L. Clark, D. R. Conradson, F. J. Espinosa-Faller, J. S. Lezama Pacheco, M. B. Martucci, D. Nordlund, G. T. Seidler, and J. A. Valdez, “Anomalous dispersion and band gap reduction in UO_{2+x} and its possible coupling to the coherent polaronic quantum state,” *Nuclear Instruments & Methods in Physics Research B*, vol. 374, pp. 45–50, 2016.

[24] I. Arts, R. Saniz, G. Baldinozzi, G. Leinders, M. Verwerft, and D. Lamoen, “Ab initio study of the adsorption of O, O_2 , H_2O and H_2O_2 on UO_2 surfaces using DFT+U and non-collinear magnetism,” *Journal of Nuclear Materials*, vol. 599, 2024.

[25] W. Thomas, F. Wilhelm, S. Langridge, L. M. Harding, C. Bell, R. Springell, S. Friedemann, R. Caciuffo, and G. H. Lander, “Absence of induced ferromagnetism in epitaxial uranium dioxide thin films,” *Physical Review B*, vol. 109, no. 6, 2024.

[26] R. Saniz, G. Baldinozzi, I. Arts, D. Lamoen, G. Leinders, and M. Verwerft, “Charge order, frustration relief, and spin-orbit coupling in U_3O_8 ,” *Physical Review Materials*, vol. 7, no. 5, 2023.

[27] E. Lawrence Bright, L. Xu, L. M. Harding, R. Springell, A. C. Walters, M. Sundermann, M. Garcia-Fernandez, S. Agrestini, R. Caciuffo, G. van der Laan, and G. H. Lander, “Resonant inelastic X-ray scattering from U_3O_8 and UN,” *Journal of Physics: Condensed Matter*, vol. 35, no. 17, 2023.

[28] A. Miskowiec, T. Spano, Z. E. Brubaker, J. L. Niedziela, D. L. Abernathy, R. D. Hunt, and S. Finkeldei, “Comment on ‘Resonant inelastic x-ray scattering from U_3O_8 and UN’,” *Journal of Physics: Condensed Matter*, vol. 36, no. 50, 2024.

[29] S. D. Conradson, D. Manara, F. Wastin, D. L. Clark, G. H. Lander, L. A. Morales, J. Rebizant, and V. V. Rondinella, “Local structure and charge distribution in the UO_2 – U_4O_9 system,” *Inorganic chemistry*, vol. 43, no. 22, pp. 6922–6935, 2004.

[30] G. El Jamal, T. Gouder, and M. Jonsson, “Monitoring the gradual change in oxidation state during surface oxidation or reduction of uranium oxides by photoemission spectroscopy of the 5f states,” *Journal of Nuclear Materials*, vol. 560, 2022.

[31] J. M. Elorrieta, A. Milena-Pérez, J.-F. Vigier, L. J. Bonales, and N. Rodríguez-Villagra, “New insights into the structural transition from UO_{2+x} to U_3O_7 by quantitative Raman spectroscopy,” *Physical Chemistry Chemical Physics*, vol. 24, pp. 28394–28402, 2022.

[32] G. Leinders, O. G. Grendal, I. Arts, R. Bes, I. Prozheev, S. Orlat, A. Fitch, K. Kvashnina, and M. Verwerft, “Refinement of the uranium dispersion corrections from anomalous diffraction,” *Journal of Applied Crystallography*, vol. 57, no. 2, pp. 284–295, 2024.

[33] J. Lewis, R. Springell, C. Bell, R. Nicholls, J. Wasik, L. Harding, M. Gupta, J. Pakarinen, G. Baldinozzi, D. Andersson, X. Guo, and S. D. Conradson, “Charge-lattice coupling and the dynamic structure of the U–O distribution in UO_{2+x} ,” *Frontiers in Nuclear Engineering*, vol. 3, 2024.

[34] National Nuclear User Facility - Facility for Radioactive Material Surfaces (FaRMS), University of Bristol (UK), <https://nnuf-farms.bristol.ac.uk/>.

[35] R. Springell, E. Lawrence Bright, D. A. Chaney, L. M. Harding, C. Bell, R. C. C. Ward, and G. H. Lander, “A review of uranium-based thin films,” *Advances in Physics*, vol. 71, no. 3-4, pp. 87–165, 2022.

[36] S. Rennie, “Engineering UO_2 thin films to investigate nuclear fuel behaviour (*in- and ex-operando*)”. PhD thesis, University of Bristol, School of Physics, 2018.

[37] J. E. Stubbs, A. M. Chaka, E. S. Ilton, C. A. Biwer, M. H. Engelhard, J. R. Bargar, and P. J. Eng, “ UO_2 oxidative corrosion by nonclassical diffusion,” *Physical Review Letters*, vol. 114, p. 246103, 2015.

[38] S. R. Spurgeon, M. Sassi, C. Ophus, J. E. Stubbs, E. S. Ilton, and E. C. Buck, “Nanoscale oxygen defect gradients in UO_{2+x} surfaces,” *PNAS*, vol. 116, no. 35, p. 17181–17186, 2019.

[39] N. Fairley, V. Fernandez, M. Richard-Plouet, C. Guillot-Deudon, J. Walton, E. Smith, D. Flahaut, M. Greiner, M. Biesinger, S. Tougaard, D. Morgan, and J. Baltrusaitis, “Systematic and collaborative approach to problem solving using X-ray photoelectron spectroscopy,” *Applied Surface Science Advances*, vol. 5, p. 100112, 2021.

[40] E. S. Ilton and P. S. Bagus, “XPS determination of uranium oxidation states,” *Surface and Interface Analysis*, vol. 43, pp. 1549–1560, 2011.

[41] E. S. Ilton, Y. Du, J. E. Stubbs, P. J. Eng, A. M. Chaka, J. R. Bargar, C. J. Neline, and P. S. Bagus, “Quantifying small changes in uranium oxidation states using XPS of a shallow core level,” *Physical Chemistry Chemical Physics*, vol. 19, no. 45, 2017.

[42] K. I. Maslakov, Y. A. Teterin, A. J. Popel, A. Y. Teterin, K. E. Ivanov, S. N. Kalmykov, V. G. Petrov, R. Springell, T. B. Scott, and I. Farnan, “XPS study of the surface chemistry of UO_2 (111) single crystal film,” *Applied Surface Science*, vol. 433, pp. 582–588, 2018.

- [43] E. Lawrence Bright, S. Rennie, M. Cattelan, N. A. Fox, D. T. Goddard, and R. Springell, “Epitaxial UN and α -U₂N₃ thin films,” *Thin Solid Films*, vol. 661, 2018.
- [44] L. M. Harding, E. Lawrence Bright, J. Laverock, D. T. Goddard, and R. Springell, “Epitaxial stabilisation of uranium silicide line compounds,” *Thin Solid Films*, vol. 768, 2023.
- [45] J. H. Scofield, “Hartree-Slater subshell photoionization cross-sections at 1254 and 1487 eV,” *Journal of Electron Spectroscopy and Related Phenomena*, vol. 8, pp. 129–137, 1976.
- [46] B. Ravel and M. Newville, “ATHENA, ARTEMIS, HEPHAESTUS: Data analysis for X-ray absorption spectroscopy using IFEFFIT,” *Journal of Synchrotron Radiation*, vol. 12, pp. 537–541, 2005.
- [47] S. I. Zabinsky, J. J. Rehr, A. Ankudinov, R. C. Albers, and M. J. Eller, “Multiple-scattering calculations of X-ray-absorption spectra,” *Physical Review B*, vol. 52, pp. 2995–3009, 1995.
- [48] S. A. Barrett, A. J. Jacobson, B. C. Tofield, and B. E. F. Fender, “The preparation and structure of barium uranium oxide BaUO_{3+x},” *Acta Crystallographica B: Structural Science, Crystal Engineering and Materials*, vol. 38, pp. 2775–2781, 1982.
- [49] R. Springell, S. Rennie, L. Costelle, J. Darnbrough, C. Stitt, E. Cocklin, C. Lucas, R. Burrows, H. Sims, D. Wermeille, J. Rawle, C. Nicklin, W. Nuttall, T. Scott, and G. Lander, “Water corrosion of spent nuclear fuel: radiolysis driven dissolution at the UO₂/water interface,” *Faraday Discussions*, vol. 180, pp. 301–311, 2015.
- [50] S. Rennie, E. Lawrence Bright, J. Sutcliffe, J. Darnbrough, R. Burrows, J. Rawle, C. Nicklin, G. Lander, and R. Springell, “The role of crystal orientation in the dissolution of UO₂ thin films,” *Corrosion Science*, vol. 145, pp. 162–169, 2018.

Supplemental Information

S1 Additional EXAFS Figures

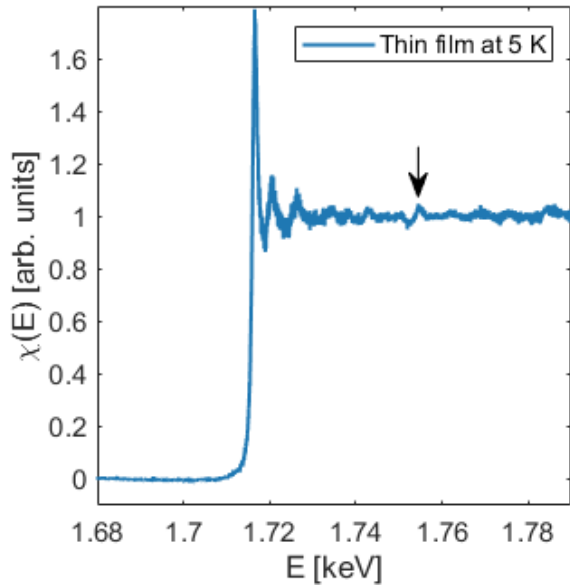


Figure S1: Normalised U L₃ edge absorption spectra for SN1 at 5 K. Highlighted with a black arrow is a diffraction peak.

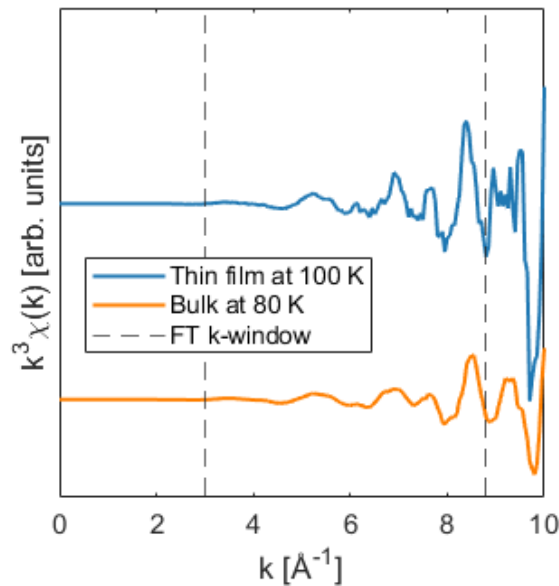


Figure S2: $\chi(k)$ for SN1 (blue, 100K) and bulk UO₂ (orange, 80K). Dashed vertical lines show the Δk Fourier transform window.

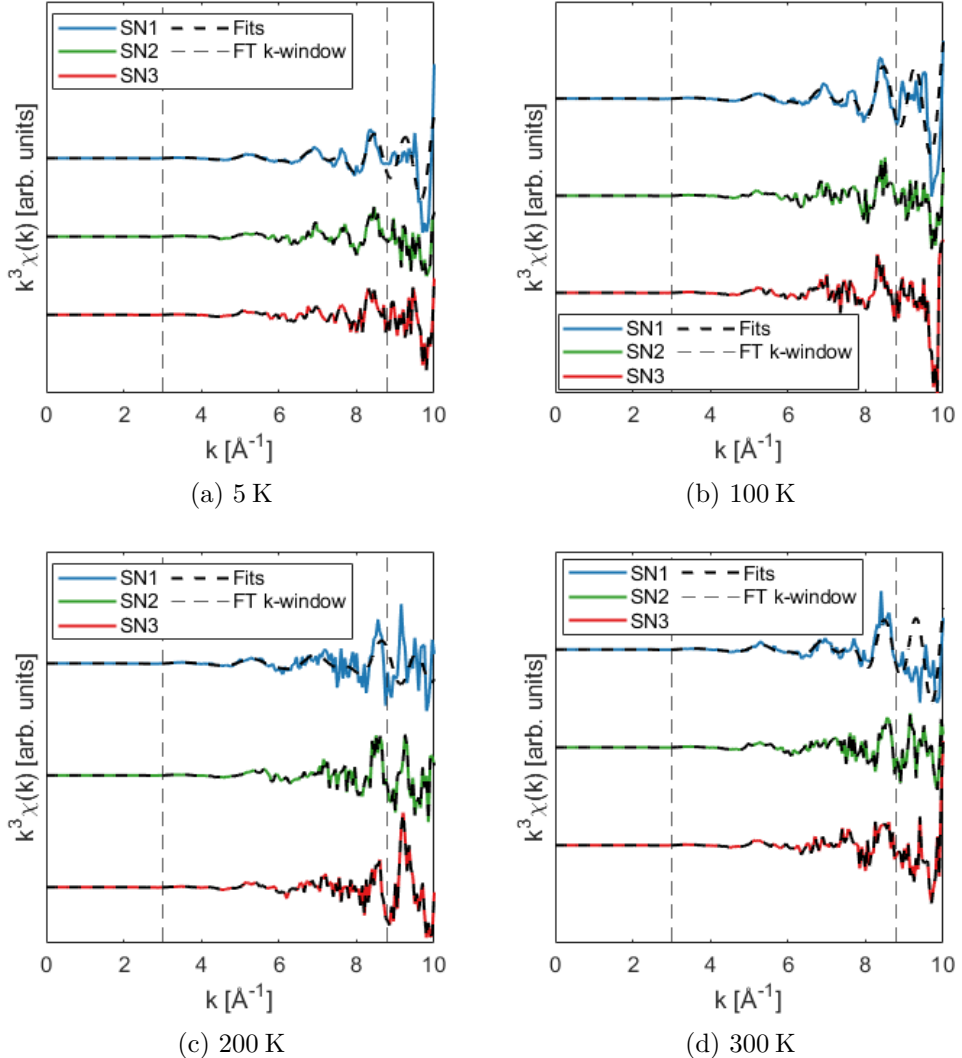


Figure S3: $\chi(k)$ absorption data plotted for samples SN1 – 3 for temperatures of 5, 100, 200, and 300 K. Each spectra is plotted scaled by k^3 , magnifying the high- k oscillations. Included in each plot is a representation of the same R-space multiple-scattering path fit from the $\chi(R)$ data. The Δk Fourier transform window range is denoted by the dashed vertical lines.

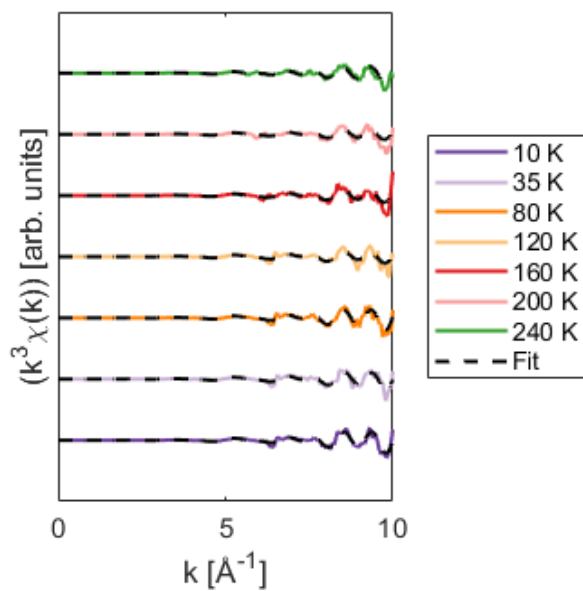


Figure S4: $\chi(k)$ absorption data plotted for sample SN4 for temperatures of 10 – 240 K. Each spectra is plotted scaled by k^3 , to magnify the high- k oscillations. Included in each plot is a representation of the same R-space multiple-scattering path fit from the $\chi(R)$ data.

S2 EXAFS Fitting Parameters

Temperature [K]	Path	ΔE_0 [eV]	σ^2 [\AA^2]	R [\AA]	Fitting	ΔR [\AA]	FT Δk [\AA^{-1}]
5	U-O ₁		0.0051 \pm 0.0012	2.366 \pm 0.017	1.0 – 5.0	3 – 8.8	
	U-U ₁	4.58	0.0019 \pm 0.0018	3.891 \pm 0.016			
	U-O ₂		0.0051 \pm 0.0012	4.534 \pm 0.039			
100	U-O ₁		0.0056 \pm 0.0017	2.374 \pm 0.024			
	U-U ₁	6.32	0.0010 \pm 0.0009	3.894 \pm 0.021			
	U-O ₂		0.0056 \pm 0.0017	4.524 \pm 0.055			
200	U-O ₁		0.0061 \pm 0.0023	2.367 \pm 0.027			
	U-U ₁	5.38	0.0058 \pm 0.0031	3.805 \pm 0.053			
	U-O ₂		0.0061 \pm 0.0023	4.381 \pm 0.084			
300	U-O ₁		0.0068 \pm 0.0018	2.368 \pm 0.023			
	U-U ₁	4.58	0.0015 \pm 0.0010	3.891 \pm 0.020			
	U-O ₂		0.0068 \pm 0.0018	4.518 \pm 0.055			

Table S1: $\chi(R)$ fit parameters for sample SN1.

Temperature [K]	Path	ΔE_0 [eV]	σ^2 [\AA^2]	R [\AA]	Fitting	ΔR [\AA]	FT Δk [\AA^{-1}]
5	U-O ₁		0.0084 \pm 0.0024	2.346 \pm 0.033	1.0 – 5.0	3 – 8.8	
	U-U ₁	4.95	0.0019 \pm 0.0018	3.864 \pm 0.028			
	U-O ₂		0.0084 \pm 0.0024	4.462 \pm 0.075			
100	U-O ₁		0.0094 \pm 0.0012	2.333 \pm 0.016			
	U-U ₁	3.29	0.0029 \pm 0.0009	3.848 \pm 0.014			
	U-O ₂		0.0094 \pm 0.0012	4.433 \pm 0.036			
200	U-O ₁		0.0097 \pm 0.0022	2.309 \pm 0.035			
	U-U ₁	0.84	0.0073 \pm 0.0029	3.801 \pm 0.041			
	U-O ₂		0.0097 \pm 0.0022	4.402 \pm 0.081			
300	U-O ₁		0.0069 \pm 0.0017	2.349 \pm 0.020			
	U-U ₁	4.57	0.0064 \pm 0.0024	3.826 \pm 0.038			
	U-O ₂		0.0069 \pm 0.0017	4.395 \pm 0.062			

Table S2: $\chi(R)$ fit parameters for sample SN2.

Temperature [K]	Path	ΔE_0 [eV]	σ^2 [\AA^2]	R [\AA]	Fitting ΔR [\AA]	FT Δk [\AA^{-1}]
5	U-O ₁		0.0082 \pm 0.0016	2.344 \pm 0.026	1.0 – 5.0	3 – 8.8
	U-U ₁	1.92	0.0028 \pm 0.0017	3.872 \pm 0.021		
	U-O ₂		0.0082 \pm 0.0016	4.490 \pm 0.053		
100	U-O ₁		0.0084 \pm 0.0013	2.390 \pm 0.015		
	U-U ₁	6.03	0.0022 \pm 0.0010	3.895 \pm 0.015		
	U-O ₂		0.0084 \pm 0.0013	4.474 \pm 0.037		
200	U-O ₁		0.0120 \pm 0.0026	2.356 \pm 0.030		
	U-U ₁	5.45	0.0109 \pm 0.0052	3.839 \pm 0.059		
	U-O ₂		0.0120 \pm 0.0026	4.388 \pm 0.093		
300	U-O ₁		0.0108 \pm 0.0017	2.314 \pm 0.021		
	U-U ₁	0.17	0.0049 \pm 0.0021	3.851 \pm 0.021		
	U-O ₂		0.0108 \pm 0.0017	4.532 \pm 0.046		

Table S3: $\chi(R)$ fit parameters for sample SN3.

Temperature [K]	Path	ΔE_0 [eV]	σ^2 [\AA^2]	R [\AA]	Fitting ΔR [\AA]	FT Δk [\AA^{-1}]
10	U-O ₁		0.0126 \pm 0.0018	2.330 \pm 0.024	1.0 – 5.0	3.0 – 8.8
	U-U ₁	3.93	0.0064 \pm 0.0017	3.841 \pm 0.026		
	U-O ₂		0.0126 \pm 0.0018	4.427 \pm 0.057		
35	U-O ₁		0.0123 \pm 0.0021	2.336 \pm 0.024		
	U-U ₁	4.74	0.0075 \pm 0.0025	3.845 \pm 0.033		
	U-O ₂		0.0123 \pm 0.0021	4.405 \pm 0.065		
80	U-O ₁		0.0126 \pm 0.0022	2.339 \pm 0.024		
	U-U ₁	4.95	0.0064 \pm 0.0022	3.852 \pm 0.029		
	U-O ₂		0.0126 \pm 0.0022	4.419 \pm 0.063		
120	U-O ₁		0.0129 \pm 0.0024	2.348 \pm 0.026		
	U-U ₁	6.44	0.0097 \pm 0.0038	3.864 \pm 0.044		
	U-O ₂		0.0129 \pm 0.0024	4.414 \pm 0.077		
160	U-O ₁		0.0133 \pm 0.0023	2.355 \pm 0.028		
	U-U ₁	4.06	0.0092 \pm 0.0029	3.861 \pm 0.041		
	U-O ₂		0.0133 \pm 0.0023	4.434 \pm 0.074		
200	U-O ₁		0.0152 \pm 0.0025	2.357 \pm 0.034		
	U-U ₁	5.11	0.0112 \pm 0.0032	3.867 \pm 0.046		
	U-O ₂		0.0152 \pm 0.0025	4.470 \pm 0.084		
240	U-O ₁		0.0189 \pm 0.0016	2.358 \pm 0.017		
	U-U ₁	4.84	0.0086 \pm 0.0013	3.858 \pm 0.018		
	U-O ₂		0.0189 \pm 0.0016	4.44 \pm 0.042		

Table S4: $\chi(R)$ fit parameters for sample SN4.